

# Device architecture for efficient, low-hysteresis flexible perovskite solar cells: Replacing TiO<sub>2</sub> with C<sub>60</sub> assisted by polyethylenimine ethoxylated interfacial layers

Jaewon Ha<sup>a</sup>, Hoyeon Kim<sup>a</sup>, Hyunwoo Lee<sup>a</sup>, Kyung-Geun Lim<sup>b</sup>, Tae-Woo Lee<sup>c</sup>, Seunghyup Yoo<sup>a,\*</sup>

<sup>a</sup> School of Electrical Engineering, Korea Advanced Institute of Science and Technology (KAIST), 291 Daehak-ro, Yuseong-gu, Daejeon 34141, Republic of Korea

<sup>b</sup> Department of Materials Science and Engineering, Pohang University of Science and Technology (POSTECH), 77 Cheongam-ro, Nam-gu, Pohang, Gyeongbuk 37673, Republic of Korea

<sup>c</sup> Department of Materials Science and Engineering, Seoul National University, 1 Gwanak-ro, Gwanak-gu, Seoul 08826, Republic of Korea

## ARTICLE INFO

### Keywords:

Perovskite solar cell  
Low-temperature process  
Flexible solar cell  
Low-hysteresis  
Interface engineering

## ABSTRACT

We here report methylammonium lead-iodide-based perovskite solar cells (psSCs) in which a TiO<sub>2</sub> layer (a *de-facto* electron transport layer of psSCs) is replaced with a layer of C<sub>60</sub> evaporated onto indium tin oxide layers covered with polyethylenimine ethoxylated (PEIE) layers. Unlike TiO<sub>2</sub> layers requiring a high-temperature sintering, C<sub>60</sub> is deposited while the substrate is held at room temperature, making it compatible with various plastic substrates for flexible psSCs. The PEIE layers are shown to play key roles, not only as an electron-collecting interfacial layer but also as a surface modifier that helps maintain the integrity of the C<sub>60</sub> layers during spin-coating of the perovskite active layers. Using the proposed device architecture, we demonstrate flexible psSCs that exhibit power conversion efficiency as high as 13.3% with low hysteresis.

## 1. Introduction

With the increasing awareness of environment pollution and energy crisis, solar energy has been recognized as an important renewable source of energy, which can be converted and stored through various technologies such as photoelectrochemical cell, photocatalysis [1,2], and photovoltaic (PV) cells. Organic-inorganic lead halide perovskite solar cell (psSC) technology, in particular, has recently gained immense attention as one of the most promising low-cost PV energy-generation technologies [3–7]. With intensive efforts devoted to this emerging PV technology, the power conversion efficiency (PCE) of psSCs has dramatically improved from 3.8% [8] to 22.1% [9] in the past few years. Growing highly crystalline perovskite photoactive layers was shown to be a critical factor in realizing high-PCE psSCs. In addition, most psSCs in a normal configuration, where the cathode is on the substrate side, generally contain a hole blocking and electron transporting layer (ETL) of compact and/or mesoporous titanium oxide (TiO<sub>2</sub>) layers. These layers, however, require a high-temperature around 450–500 °C for sintering process [8,10–12], making it challenging to realize flexible psSCs. Initial efforts were thus made based on a mesoporous-TiO<sub>2</sub>-free inverted planar geometry, in which “inverted” refers to a case where an anode is placed on the substrate. Such trials

include a device geometry where a conducting polymer of poly(3,4-ethylenedioxythiophene) polystyrene sulfonate (PEDOT:PSS) or its variant is used as a bottom hole-transporting buffer layer and fullerene derivatives serve as a top electron transport layer [13–16]. Nevertheless, those flexible psSCs exhibited PCE < 10%; this may be regarded consistent with the fact that the PCEs of the psSCs in an inverted planar geometry have been found lower than those of the psSCs in a normal geometry in most of the reports found in the literature [17,18]. Note that having both flexibility and high efficiency could be a critical feature that could differentiate psSCs from other PV technologies. It would thus be highly beneficial to find an alternative ETL processable at a temperature compatible with most plastic substrates. It would be even better, if it could work with normal geometry, in which a solution-based growth of high-quality perovskite active layers could be possible without damaging the underlying ETL. In this regard, various low-temperature processes were proposed for ETL with normal geometry [7,19–21].

Another issue that is important in psSCs is the frequently observed hysteresis behavior in their current density-voltage (*J-V*) hysteresis, which leads to an undesirable PCE difference depending on voltage scan direction and scan rate [22–25]. In general, low PCE due to decrease in the fill factor is observed with forward scan (short-circuit to

\* Corresponding author.

E-mail address: [syoo@ee.kaist.ac.kr](mailto:syoo@ee.kaist.ac.kr) (S. Yoo).

open-circuit), and a fast scan rate tends to increase the PCE difference between forward and reverse scan (open-circuit to short-circuit) [24,25]. Because of its significant practical implications, it is critically important to make sure any new structure or layer configuration, at the least, would not aggravate; but much better, would reduce or suppress this hysteresis effect.

Here, we explore flexible psSCs in a normal geometry for which the bottom ETL of TiO<sub>2</sub> is replaced with evaporated C<sub>60</sub>, well-known in organic electronics for its excellent electron transport properties [26,27]. A previous report by Kim et al. [28] suggested that C<sub>60</sub> can work as an ETL also in the psSCs although it was demonstrated as an ETL prepared on top of perovskite materials in fully vacuum-evaporated psSCs. This left a question about whether it would also work as a bottom ETL in psSCs with solution-processed perovskite layers. In a recent report by Snaith and his coworkers [29], a solution-processed C<sub>60</sub> film was employed to replace a bottom TiO<sub>2</sub> layer, suggesting that it might be plausible. Recently, Yoon et al. [30] reported that thermally evaporated C<sub>60</sub> can indeed work as a bottom ETL, further corroborating the potential of C<sub>60</sub> films as an alternative ETL. Nevertheless, the typical two-step spin-coating method could not be used in both of these studies; instead, the deposition of the lead iodide (PbI<sub>2</sub>) layer was done via thermal evaporation in the former, and one-step spin-coating with diethyl ether dripping method was used in the latter, both of which were motivated mainly by a concern about partial dissolution of C<sub>60</sub> films during spin-coating of PbI<sub>2</sub>. It would thus be helpful to develop a device architecture that is based on C<sub>60</sub> but can work with common two-step spin-coating method as well.

In this study, it turns out that C<sub>60</sub> layers deposited on a bare indium tin oxide (ITO) layer are subject to damage during the spin-coating process for methylammonium lead iodide (CH<sub>3</sub>NH<sub>3</sub>PbI<sub>3</sub>; MAPbI<sub>3</sub>) based perovskite photoactive layers. However, those grown on ITOs coated with polyethylenimine ethoxylated (PEIE) [31] are shown to keep their film integrity. It is found that they work not only as ETLs and but also as effective templates for growth of high-quality MAPbI<sub>3</sub>-based perovskite layers. With this method, we demonstrate flexible psSCs with efficiency as high as 13.3% and low hysteresis.

## 2. Experimental

A schematic device structure and energy band diagram [13,30,32,33] of the proposed psSC device and the molecular structure of key materials used therein are shown in Fig. 1(a)–(c), respectively. It

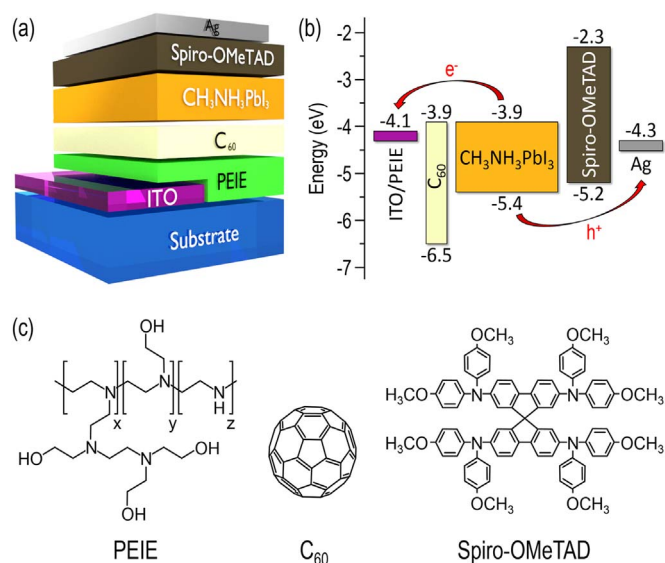


**Fig. 1.** (a) Schematic device structure and (b) energy band diagram of the proposed perovskite solar cell (psSC). (c) Molecular structure of the materials used in this work.

is based on a conventional psSC structure [34] except for the fact that a thermally evaporated C<sub>60</sub> layer is herein used as an ETL instead of mesoporous TiO<sub>2</sub> layers. As a photoactive layer, MAPbI<sub>3</sub>-based perovskite films were prepared using the so-called two-step spin-coating method [13], which consists of sequential spin-coating of PbI<sub>2</sub> and methylammonium iodide (CH<sub>3</sub>NH<sub>3</sub>I; MAI) solutions. For a cathodic interfacial layer, PEIE film was inserted between ITO and the C<sub>60</sub> layer [31].

The PEIE solution was diluted by mixing PEIE (Sigma-Aldrich) with 2-methoxyethanol to a weight concentration of 0.4 wt%, as described by Zhou et al. [31]. Then, PbI<sub>2</sub> (Sigma-Aldrich, 99%) and MAI (1-Material, 99.5%) were dissolved in *N,N*-dimethylformamide (DMF, Sigma-Aldrich, anhydrous, 99.8%) at a concentration of 462 mg/mL and 2-propanol (IPA, Sigma-Aldrich, anhydrous, 99.5%) at a concentration of 20 mg/mL, respectively. The PbI<sub>2</sub> solution was placed on a hot plate held at 100 °C during the entire spin-coating process. Next, 2,2',7,7'-tetrakis(*N,N*-di-*p*-methoxyphenylamine)-9,9'-spirobifluorene (spiro-OMeTAD, Derthon, 99.5%) was dissolved in 72.3 mg/mL chlorobenzene (Sigma-Aldrich, anhydrous, 99.8%). Then 28.8 μL/mL of 4-tert-butylpyridine and 17.5 μL/mL of lithium bis(trifluoromethylsulfonyl)imide (Li-TFSI, Sigma-Aldrich) solution (520 mg/mL Li-TFSI in acetonitrile, 99.8%) were added 30 min before spin-coating.

ITO-coated substrates (AMG glass, 10 Ω/sq. for glass and PECF-IP, Pecell Technologies Inc., 15 Ω/sq. for plastic substrates) were sequentially cleaned by ultrasonication using detergent, deionized water, acetone, and isopropanol for 20 min each. The ITO-coated plastic substrates were based on polyethylene naphthalate (PEN; 200 μm in thickness). Before the cleaning process, the half of ITO pre-coated on a 25×25 mm<sup>2</sup> substrate was patterned out by wet etching process to later define the device area by the overlapped area between ITO and metal cathodes, which were typically about 0.1 cm<sup>2</sup>. The cleaned-substrates were treated with air plasma (PDC-32G, Harrick Plasma) for 5 min. In order to avoid bending during the spin-coating process, the flexible PEN substrates were attached to a temporary carrier glass. The PEIE solution was spin-coated onto a plasma-cleaned ITO substrate at 5000 r.p.m. for 55 s and annealed on a hotplate at 100 °C for 10 min, in ambient air. The PEIE-coated ITO substrates were then loaded into a vacuum thermal evaporator (HS-1100, Digital Optics & Vacuum, < 10<sup>-6</sup> Torr) for deposition of the C<sub>60</sub> (Niche, 99.9%) ETL (25 nm thick), which was shown to decrease to 15 nm after spin-coating of the PbI<sub>2</sub> solution. The C<sub>60</sub>-evaporated substrates were transferred to the outside of the vacuum thermal evaporator for spin-coating of the perovskite photoactive layers and hole transporting layers (HTLs) [13,34]. Subsequently, PbI<sub>2</sub> solution, heated to 100 °C, was spin-coated on a C<sub>60</sub> layer at 8000 r.p.m. for 30 s, and then annealed on a hotplate at 100 °C for 5 min. After the substrates were cooled to room temperature (RT), the MAI solution was spin-coated at 3000 r.p.m. for 30 s and annealed at 100 °C for 5 min. After annealing, a dark brown MAPbI<sub>3</sub> film was formed. Spiro-OMeTAD solution was then spin-coated onto the MAPbI<sub>3</sub> perovskite layer at 4000 r.p.m. for 20 s and dried without any additional thermal annealing. Spin coating and annealing of the PbI<sub>2</sub>, MAI, and spiro-OMeTAD layers were all done inside an environment-controlled chamber, which was maintained at relative humidity (RH) of 30%. These samples were then loaded into the vacuum thermal evaporator for deposition of the silver (Ag, Ulet, 99.99%) layers as top anodes.

The *J-V* characteristics were measured with a sourcemeter unit (Keithley 2611A) under 100 mW/cm<sup>2</sup> illumination (AM1.5G) from a spectral response system (CEP-25ML, Bunkoukeiki) with the uniform irradiation area larger than 27×27 mm<sup>2</sup>. The irradiance of the incident light was verified periodically using a calibrated Si photodiode (BS-520BK, Bunkoukeiki). Measurements of *J-V* proceeded under the following conditions: voltage scan step of 10 mV, and scan delay time of 50 ms between measurement points (scan rate of 0.2 V/s) for reverse scan (from open-circuit to short-circuit) and forward scan (from short-

circuit to open-circuit). External quantum efficiency (EQE) was measured using a spectral response system (CEP-25ML, Bunkoukeiki) in direct current mode with the regulated irradiance of  $50 \mu\text{W}/\text{cm}^2$  for all the wavelengths used. During the measurements, devices were kept inside a compact vacuum chamber, which had a quartz window for light illumination. PV measurements were done using an aperture, which has a shape and area close to (but smaller than) those of the samples. The electrochemical impedance spectroscopy (EIS) was carried out with a built-in frequency response analyzer (FRA)-equipped electrochemical workstation (ZIVE SP1, WonATech), under AM1.5G illumination from the spectral response system (CEP-25ML, Bunkoukeiki) at three different forward bias of 0 V, 0.5 V, and open-circuit voltage ( $V_{oc}$ ) with the frequency ranging from 1 MHz to 1 Hz (AC amplitude of 10 mV). Measurement results were fitted using ZMAN EIS analysis software to obtain equivalent circuit and resistive parameters of psSCs. The bending-cycle test of psSC was done with a custom-made cyclic bending tester in which one can adjust the number of bending cycles and the radius of curvature [35]. Raman spectra near the pentagonal pinch mode  $A_g(2)$  [36] (wavenumber range between 1300 and  $1500 \text{ cm}^{-1}$ ) were taken using a Raman Spectroscopy System (LabRam ARAMIS, Horiba Jobin-Yvon) having an Ar-ion laser source (514.532 nm, 10 mW). X-ray diffraction (XRD) measurement for the perovskite thin films was done with a multi-purpose, thin-film X-ray diffractometer (D/MAX-2500, Rigaku) equipped with a Cu  $K\alpha$  ( $\lambda=0.15418 \text{ nm}$ ) X-ray tube operated at 40 kV and 300 mA with a scan step of  $0.01^\circ$  and scan range of  $10\text{--}50^\circ$ . X-ray photoelectron spectroscopy (XPS) measurements were performed with a Sigma Probe spectrometer (Thermo Scientific) equipped with a micro-focusing monochromatic X-ray source (Al  $K\alpha$ , 1486.7 eV). The pressure in the analysis chamber was around  $10^{-9}$  Torr and energy resolution was 0.47 eV. To eliminate the surface charging effects, all spectra were calibrated to their corresponding C 1s core level of 285.3 eV as a reference [37]. Analyses of XPS peaks were performed with an XPSPEAK4.1 program.

### 3. Results and discussion

Fig. 2(a), showing the film morphologies of  $\text{PbI}_2$  films spin-coated on  $\text{C}_{60}$ , does indicate that it will be challenging to use  $\text{C}_{60}$  alone as a bottom ETL in the two-step spin-coating method. From both optical microscope and SEM images, one can easily tell that there are severe spatial non-uniformities in  $\text{C}_{60}/\text{PbI}_2$  films. This suggests that the integrity of the  $\text{C}_{60}$  film was compromised during spin-coating of  $\text{PbI}_2$  solution on its top, which is consistent with the concern raised earlier [29]. This is in contrast with results reported in another work by Ke et al. [38], in which there was no problem using  $\text{C}_{60}$  as a bottom ETL together with spin-coating of  $\text{PbI}_2$  solution. However, our result points out that using  $\text{C}_{60}$  alone makes psSCs based thereon vulnerable to severe device-to-device variations associated with spatial non-uniformities in the  $\text{C}_{60}/\text{PbI}_2$  films. Such tendencies have very important

implications in terms of device fabrication and operation because formation of high-quality  $\text{PbI}_2$  is a prerequisite for eventual growth of the PV-quality perovskite layers in the two-step spin-coating process.

Contrary to the results obtained with the sample in which  $\text{C}_{60}$  was grown directly on ITO, spin-coating of the  $\text{PbI}_2$  solution over ITO with PEIE was shown to yield uniform  $\text{PbI}_2$  films (Fig. 2(b)). More importantly, existence of PEIE on ITO was shown to enable growth of uniform  $\text{PbI}_2$  films on top of the  $\text{C}_{60}$  as well (Fig. 2(c)). This indicates that  $\text{C}_{60}$  could work as an ETL in the two-step spin-coating method if it was used in combination with PEIE. It is also noteworthy that PEIE would work as a cathodic buffer layer as well [31], which is relevant to the normal geometry of psSCs. PEIE was shown to enhance device lifetime when used as an electron-selective buffer layer as a result of oxide passivation that tends to reduce trap-assisted interfacial recombination [32,39]. The photographs of the samples before and after spin-coating of  $\text{PbI}_2$  layers, further support the assertion that the spin-coating process causes severe damage, particularly to  $\text{C}_{60}$  layers grown directly on the bare glass part of the ITO-coated glass substrate, in which half of the ITO layer is etched out to define the active area of the device (see Fig. S1 in the Supplementary material for details). The fraction of the damaged and delaminated mixture of  $\text{C}_{60}$  and  $\text{PbI}_2$  then moves towards  $\text{C}_{60}/\text{PbI}_2$  on ITO during the spin-coating process. This leaves some areas without any  $\text{C}_{60}$  and  $\text{PbI}_2$ , or with a larger amount of them than surrounding areas, both of which cause non-uniformity in the active region.

Independent experiments done with spin-coating of DMF, the solvent of the  $\text{PbI}_2$  solution, indicate that DMF influences underlying  $\text{C}_{60}$  layers in two ways. It first dissolves away a part of the  $\text{C}_{60}$  layers, and also damages the  $\text{C}_{60}$  layers where they do not strongly adhere (i.e., those on a glass substrate in this case). This tends to yield fractures in the film (see Fig. 3(a)–(c)). Thin-film optic calculations [40] done to fit the experimental transmittance spectra of the  $\text{C}_{60}$  films before and after DMF spin-coating, indicate that 11–12 nm of the  $\text{C}_{60}$  film is dissolved by DMF in both ITO/ $\text{C}_{60}$  and ITO/PEIE/ $\text{C}_{60}$  cases. Even with this partial dissolution of the  $\text{C}_{60}$  layers, molecular characteristics of  $\text{C}_{60}$  were relatively intact by the solution process used in this work, as it can be seen from Raman spectra of  $\text{C}_{60}$  layers in both ITO/ $\text{C}_{60}$  and ITO/PEIE/ $\text{C}_{60}$  cases (Fig. S2). Moreover, those with PEIE maintained spatial uniformity over the entire area of the substrate, as it can be seen from the clear appearance of the samples, and from the similarity of microscopic morphologies of  $\text{C}_{60}/\text{PEIE}$  on ITO-coated and bare-glass parts measured, respectively, with atomic force microscopy (AFM) (Fig. S3). Both of these results illustrate that  $\text{C}_{60}$  used in combination with PEIE may still remain uniform and thick enough, even with a partial dissolution, to work properly as ETLs in the proposed psSCs.

Note that having uniform  $\text{C}_{60}/\text{PbI}_2$  layers would not be meaningful unless a high-quality  $\text{CH}_3\text{NH}_3\text{PbI}_3$  perovskite film could be grown on top of them by additional spin-coating of  $\text{CH}_3\text{NH}_3\text{I}$  solutions. X-ray diffraction (XRD) data shown in Fig. 4(a) confirm that the film integrity

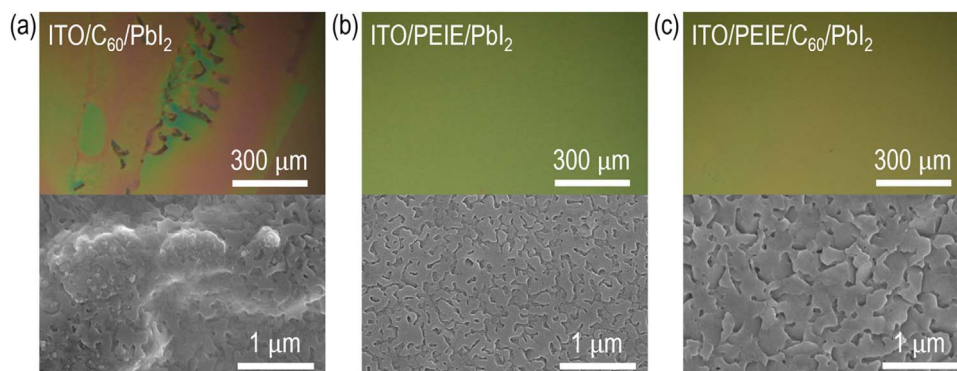
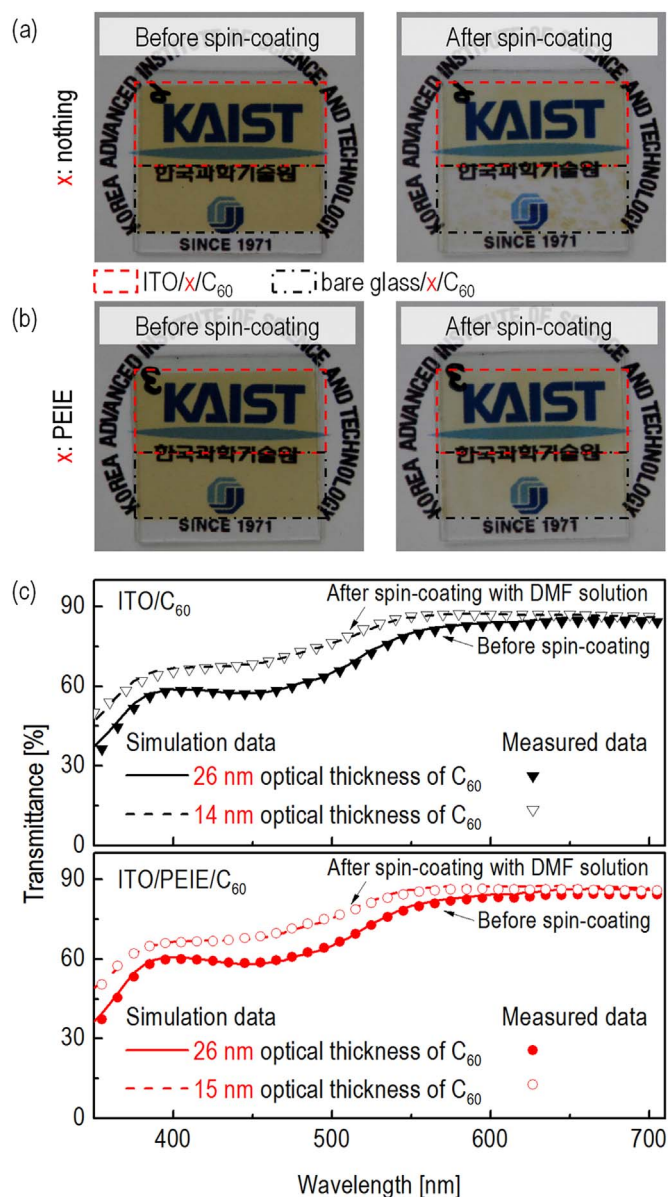


Fig. 2. Optical microscope and surface SEM images after formation of  $\text{PbI}_2$  film by spin-coating and annealing on top of (a) ITO/ $\text{C}_{60}$ , (b) ITO/PEIE, and (c) ITO/PEIE/ $\text{C}_{60}$ .



**Fig. 3.** Photograph of  $x/C_{60}$  films on ITO-coated or bare glass parts before and after spin-coating of DMF solution with  $x$  being (a) nothing and (b) PEIE, respectively. The rectangular regions indicated by the red dashed line correspond to  $x/C_{60}$  films on ITO-coated parts and those indicated by the black dash-dot line correspond to  $x/C_{60}$  films on bare glass parts. (c) Ultraviolet to visible (UV-Vis) transmittance spectra with optical simulation data, based on the thin-film optic calculation called transfer-matrix formalism (TMF) [40]. (For interpretation of the references to color in this figure legend, the reader is referred to the web version of this article.)

and spatial uniformity of the  $C_{60}/PbI_2$  layers grown on ITO/PEIE is indeed beneficial for growth of highly crystalline, pure  $CH_3NH_3PbI_3$  perovskite films. Moreover; the XRD data obtained from the perovskite films formed on top of ITO/PEIE/ $C_{60}/PbI_2$  not only show well-defined peaks consistent with previous reports [41–43], but also are free from the peaks associated with unreacted  $PbI_2$ . This is in clear contrast with the cases where perovskite films formed on top of ITO/PEIE/ $PbI_2$  or ITO/ $C_{60}/PbI_2$ ; both of which show diffraction peaks associated with  $PbI_2$ , which would work as nothing but impurities in devices.

The characteristics of the perovskite films were further studied by the XPS spectra (Fig. 4(b)–(d)). Two different core levels for C 1s and Pb 4f<sub>7/2</sub> are shown in details in Fig. 4(c) and (d), respectively. Other core-level spectra for I 3d<sub>5/2</sub>, N 1s and O 1s are also presented in Fig. S4. All of the binding energy (BE) values for main peaks well coincide

with previous reports [37,44]. The C 1s spectra show two different chemical states at the BE of 285.3 eV and 286.6 eV. The higher BE peak is assigned to the methyl group present in the perovskite materials (*i.e.*  $CH_3NH_3^+$ ), which indicates the transition from  $PbI_2$  to  $CH_3NH_3PbI_3$  [44]. In spite of less intensity than the values reported in previous works [37,44], the C 1s core-level peak at 286.6 eV of the perovskite film with ITO/PEIE/ $C_{60}$  is more intense than that of perovskite films with ITO/PEIE or ITO/ $C_{60}$ , indicating that the perovskite film with ITO/PEIE/ $C_{60}$  indeed resulted in better-quality  $CH_3NH_3PbI_3$  perovskite films than the other cases. The overall intensity drop compared with previous report can be attributed to air-annealing effect [45], which coincide with our XPS spectra of C 1s core-level. In the case of Pb 4f<sub>7/2</sub> core-level spectra, two chemical states are shown at the BE of 138.6 eV and 136.9 eV. The higher BE peak is attributed to the Pb-I bonding or  $Pb(OH)_2$  [44,45]. The second peak with the energy difference of 1.7 eV at the lower BE is assigned to the metallic lead ( $Pb^0$ ), which is considered to be induced by the reduction of  $Pb^{2+}$  due to the chemical reaction during the annealing process or by X-ray source damage during the measurement [45–48]. The metallic lead species are likely to act as non-radiative recombination centers which interrupt PV operation due to the existence of iodide vacancies in the perovskite film lattice [47]. The metallic lead peak is reduced in the perovskite film with ITO/PEIE/ $C_{60}$ , indicating that iodide vacancies in the crystal lattice were also reduced when both PEIE and  $C_{60}$  were present. Formation of small, densely packed perovskite crystals can also be seen from the SEM images of the perovskite films formed on top of ITO/PEIE/ $C_{60}/PbI_2$  (Fig. S5).

Fig. 5(a) presents the  $J$ - $V$  characteristics of psSCs with the electrode/ETL configurations under study (See Table 1 also for summary of PV performance parameters.). Almost negligible PCEs were observed for psSCs with ITO/PEIE, but without  $C_{60}$ . This can be regarded as a consequence of (i) the absence of the hole-blocking function that could be expected from  $C_{60}$  in the other devices, and/or of (ii) the presence of  $PbI_2$  impurities. Both of the devices with evaporated  $C_{60}$ , on the other hand, exhibited measurable PV characteristics. In particular, the best-performing device with ITO/PEIE/ $C_{60}$  showed PCE higher than 14% under illumination of simulated AM1.5G (1 Sun), while that with ITO/ $C_{60}$  showed a PCE of approximately 7–8%. The trend in  $J$ - $V$  characteristics and corresponding PV parameters - mainly short-circuit current density ( $J_{sc}$ ) and PCE - is also well reflected in the EQE spectra shown in Fig. 5(b), which shows the best performance for psSCs with ITO/PEIE/ $C_{60}$  and the worst for ITO/PEIE.

Most of all, psSCs with ITO/PEIE/ $C_{60}$  exhibit very little hysteresis between forward scan (FS; short-circuit to open-circuit) and reverse scan (RS; open-circuit to short-circuit) directions, which is often problematic in psSCs [22–25]. With the scan rate of 0.2 V/s (voltage scan step=10 mV; delay time=50 ms), the hysteric index (HI) [49] defined by  $(J_{RS} - J_{FS})/J_{RS}$  at  $V = 0.5 V_{oc}$  is estimated to be merely 0.029 for the best-performing ITO/PEIE/ $C_{60}$ -based psSC, while it is 0.089 for the best-performing ITO/ $C_{60}$ -based psSC (Fig. 5(a)). In addition, the ITO/PEIE/ $C_{60}$ -based psSCs are shown to exhibit little change in their PCE and low-hysteresis characteristics regardless of scan rate from 1 to 0.01 V/s (voltage scan step of 10 mV, delay time of 10–1000 ms). This is in contrast with the case of the ITO/ $C_{60}$ -based psSCs (Fig. S6) that exhibit relatively large dependence of the performance on the scan rate. The reason for the appearance of low but non-zero hysteresis, although it is still much lower than  $TiO_2$ -based psSCs [22–25], is attributed to the spiro-OMeTAD layer, which can reportedly contribute to  $J$ - $V$  hysteresis to some extent [50].

To further understand the electrical characteristics of psSCs, photo-EIS measurement has been carried out. Two capacitance steps observed in low and intermediate frequency have been reported and well interpreted recently by many other groups [50–52]. Especially, the low-frequency capacitance ( $C_{LF}$ ) was suggested as electrode polarization caused by outer contact charging, presumably originated by ion interfacial accumulation, which causes the observed current hysteresis

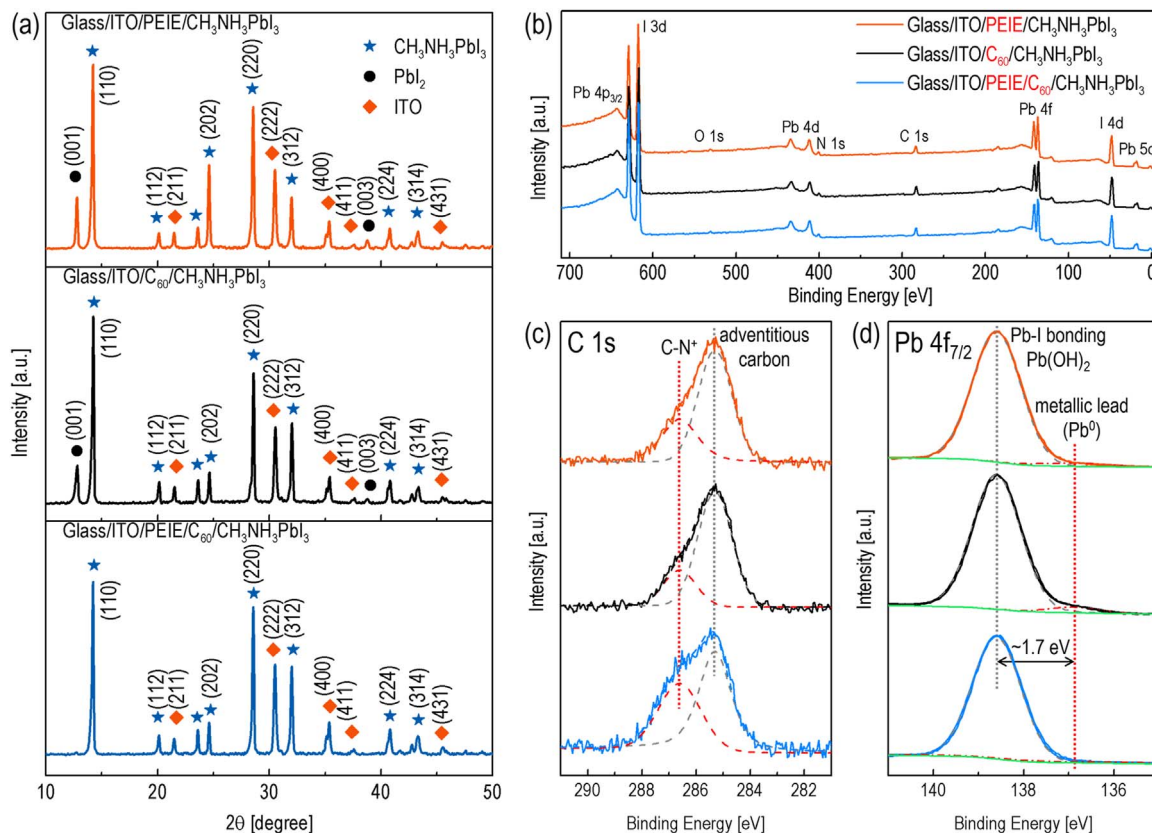


**Fig. 4.** (a) X-ray diffraction (XRD) patterns of CH<sub>3</sub>NH<sub>3</sub>PbI<sub>3</sub> perovskite films grown on the electrode/ETL combinations under study. X-ray photoelectron spectroscopy (XPS) spectra of the same: (b) overview; (c) C 1s and (d) Pb 4f<sub>7/2</sub> core-level spectra.

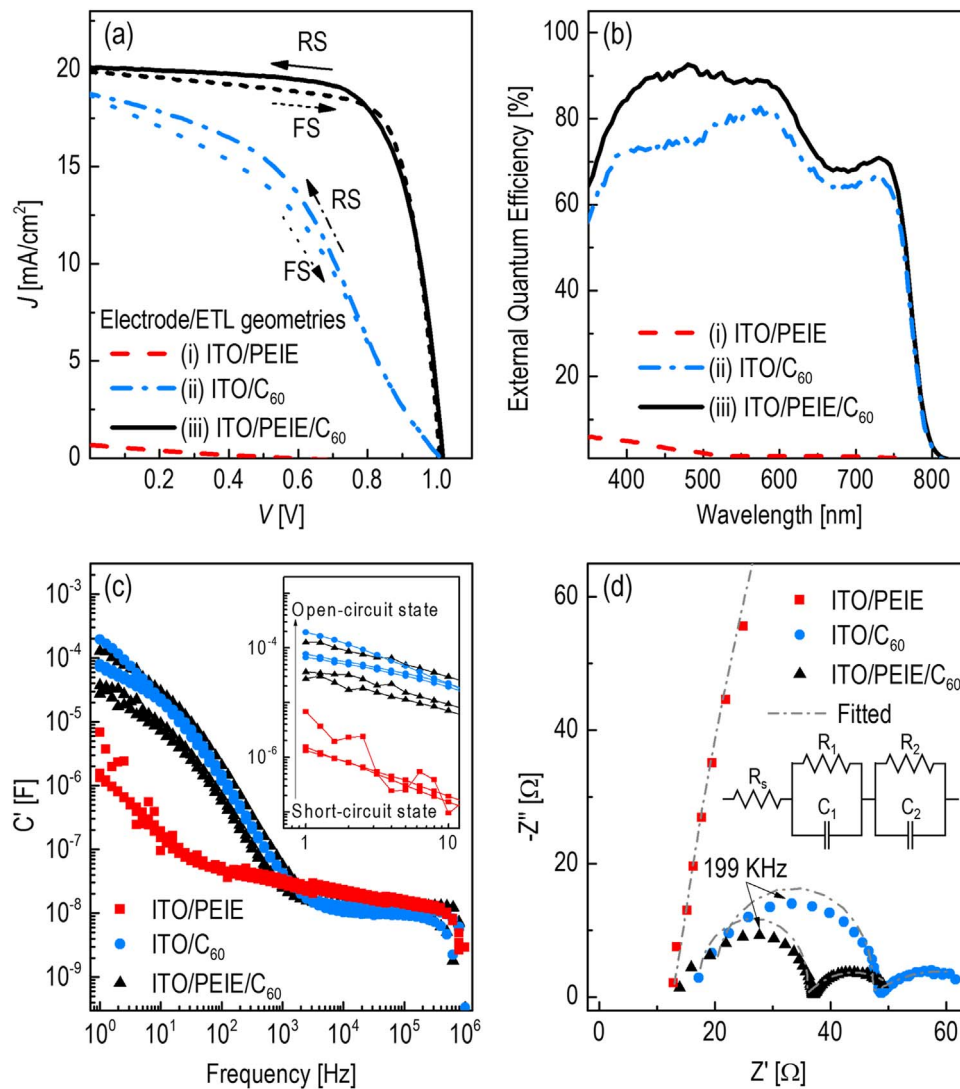
[49,51,53,54]. Photo-EIS results shown in Fig. 5(c) reveal that ITO/PEIE/C<sub>60</sub>-based psSCs have lower C<sub>LF</sub> at all of the applied bias conditions than do ITO/C<sub>60</sub>-based psSCs, consistent with the observed low HI of the proposed psSCs. At first glance, it seems that psSCs without C<sub>60</sub> have much lower C<sub>LF</sub> than psSCs with PEIE/C<sub>60</sub> at low frequency (~1 Hz). However, this is a misinterpretation because the capacitance inflection point, near the dipole polarization in intermediate frequency, shifted from 1 kHz for psSCs with PEIE/C<sub>60</sub> to 10 Hz for the psSCs without C<sub>60</sub>. This implies that another capacitance inflection point, where the electrode polarization is transformed to the dipole polarization (near 10 Hz for psSCs with PEIE/C<sub>60</sub>), also moves to lower frequency by 2 orders of magnitude for psSCs without C<sub>60</sub>, indicating that the electrode polarization is much faster by reducing chemical interactions between PEIE/C<sub>60</sub> and iodide ions in perovskite so that low-hysteresis characteristics are observed for the psSCs with PEIE/C<sub>60</sub> [50].

Fig. 5(d) shows the Nyquist impedance plots of psSCs in Fig. 5(c), which can be fitted by the equivalent circuit in the inset where R<sub>s</sub>, R<sub>1</sub> and R<sub>2</sub> represent a series resistance due to contact and wires, a charge transfer resistance at the perovskite interface, and an interfacial recombination resistance, respectively [20,55–57]. Here, two clear semicircles were observed, one in the high-frequency (low Z') and the other in the low-frequency related to R<sub>1</sub> and R<sub>2</sub>, respectively. The resistance values are summarized in Table S1. The ITO/PEIE/C<sub>60</sub>-based psSCs show lower values of R<sub>s</sub> and R<sub>1</sub> but almost the same value of R<sub>2</sub> as ITO/C<sub>60</sub>-based psSCs. ITO/PEIE-based psSCs show the highest value of R<sub>1</sub>, suggesting that ITO/PEIE/C<sub>60</sub>-based psSCs show more efficient charge transfer among all of the different psSCs. These results provide a plausible reason why ITO/PEIE/C<sub>60</sub>-based psSCs could have an increased fill factor (FF) while maintaining the same V<sub>oc</sub> as ITO/C<sub>60</sub>-based psSCs.

Furthermore, the characteristics of psSCs with ITO/PEIE/C<sub>60</sub> turn out to be much more reproducible and consistent than those of the

PEIE-free counterparts. The PV properties of the devices with ITO/PEIE/C<sub>60</sub>, obtained at RS [FS] for 35 devices from four different batches, have a relatively narrow distribution with the following average values: J<sub>sc</sub> of (19.1 ± 1.24 mA/cm<sup>2</sup>) [(19.0 ± 1.22) mA/cm<sup>2</sup>]; V<sub>oc</sub> of (1.000 ± 0.022 V) [(0.995 ± 0.020) V]; FF of 0.68 ± 0.04 [0.67 ± 0.05]; and PCE of (13.0 ± 0.9%) [(12.7 ± 1.1)%] (see Fig. S7 for the J-V characteristics of all the devices tested.). Such good reproducibility is in strong contrast with the case of ITO/C<sub>60</sub>-based psSCs, which exhibit quite a wide spread in their characteristics. All the results shown above illustrate the importance of synergetic collaboration between PEIE and C<sub>60</sub>, which serves as a low-temperature processable cathodic buffer/ETL and, at the same time, enables consistent and uniform growth of CH<sub>3</sub>NH<sub>3</sub>PbI<sub>3</sub> by the two-step spin-coating process. In addition, the psSCs based on ITO/PEIE/C<sub>60</sub> was found to hold their performance well, with a simple face-seal encapsulation [58], even after exposure to ambient air at relative humidity of 50 (± 10)% (Fig. S8). Details on encapsulation structure will be published elsewhere.

By taking full advantage of the proposed psSC, flexible psSCs were tried using ITO-coated PEN substrates. The proposed, flexible psSCs were shown to exhibit a PCE as high as 13.3%, and a HI value of 0.016 (Fig. 6(a); Table 1 for performance summary and Table 2 for comparison with the previous works in the literature), comparable to that of glass-based counterpart reference-psSC, and their device characteristics were also found to be reasonably reproducible (Fig. S9). Slightly lower PCE of the flexible psSC than that of the glass-based cell is attributed mainly to the transmittance of the PEN/ITO substrate that is lower than that of the glass/ITO substrate. This results from the high refractive index of PEN [59] increasing the reflectance at air/PEN interface and from its relatively large absorption in the spectral range 350–400 nm (See the inset of Fig. 6(b)). The effect of absorption in blue-UV range can also be seen from their EQE spectra, shown in Fig. 6(b) (see also Fig. 5(b) for comparison.). Therefore, it might be possible to further improve the performance of flexible psSCs by



**Fig. 5.** (a) Current density-voltage ( $J$ - $V$ ) characteristics of the best performing devices: psSCs on the electrode/ETL combinations under study.  $J$ - $V$  characteristics obtained at reverse scan (RS) and forward scan (FS) for the psSCs with ITO/PEIE/ $C_{60}$  and ITO/ $C_{60}$ . (b) External quantum efficiency (EQE) spectra of each of the psSCs in (a). (c) Bode plot of the real part of the capacitance ( $=C'$ ) obtained from impedance spectroscopy at three different applied bias (0 V, 0.5 V, and  $V_{oc}$ ) for the psSCs under one sun illumination. Inset shows the capacitance at low frequency (1–10 Hz). (d) Complex plane impedance plots for the psSCs at open-circuit state under one sun illumination. Symbols are the measured results and dash-dot lines correspond to the simulation results of fitting the equivalent circuit model as inset.

**Table 1**

Photovoltaic properties obtained at forward scan (FS) and reverse scan (RS) for the best performing devices with various electrode/ETL combinations (100 mW/cm<sup>2</sup>, AM1.5G, voltage scan step=10 mV, delay time=50 ms).

Substrate	Electrode/ETL	Scan direction	$J_{sc}$ [mA/cm <sup>2</sup> ]	$V_{oc}$ [V]	FF	PCE [%]	Hysteric index <sup>a</sup>
Glass	ITO/PEIE	FS	0.66	0.398	0.16	0.04	–
		RS	0.68	0.584	0.20	0.08	
	ITO/ $C_{60}$	FS	18.7	1.011	0.39	7.4	0.085
		RS	18.8	1.011	0.43	8.2	
PEN	ITO/PEIE/ $C_{60}$	FS	19.9	1.009	0.73	14.7	0.029
		RS	20.1	1.017	0.70	14.4	
	ITO/PEIE/ $C_{60}$	FS	18.0	1.016	0.70	12.8	0.016
		RS	17.9	1.020	0.73	13.3	

<sup>a</sup> The hysteric index was calculated by  $(J_{RS}-J_{FS})/J_{RS}$  at  $V=0.5 V_{oc}$  [49].

replacing PEN using plastic substrates with higher transmittance, or by adopting a simple antireflection coating. In addition, the proposed flexible psSCs were found to hold their performance well even after repeated bending at radii of curvature of 7.5 and 10 mm, which corresponds to flexural strain of 1.3% and 1% for the 200  $\mu$ m-thick PEN substrate used in this work, respectively (Fig. 6(c) and (d)). After

1000 bending cycles at strain of 1% and 1.3%, devices maintained over 90% and 80% of their initial PCE, respectively. The observed degradation of cell performance at a higher strain is attributed to the limited flexibility of ITO electrode, which is consistent with the previous reports [20,35].

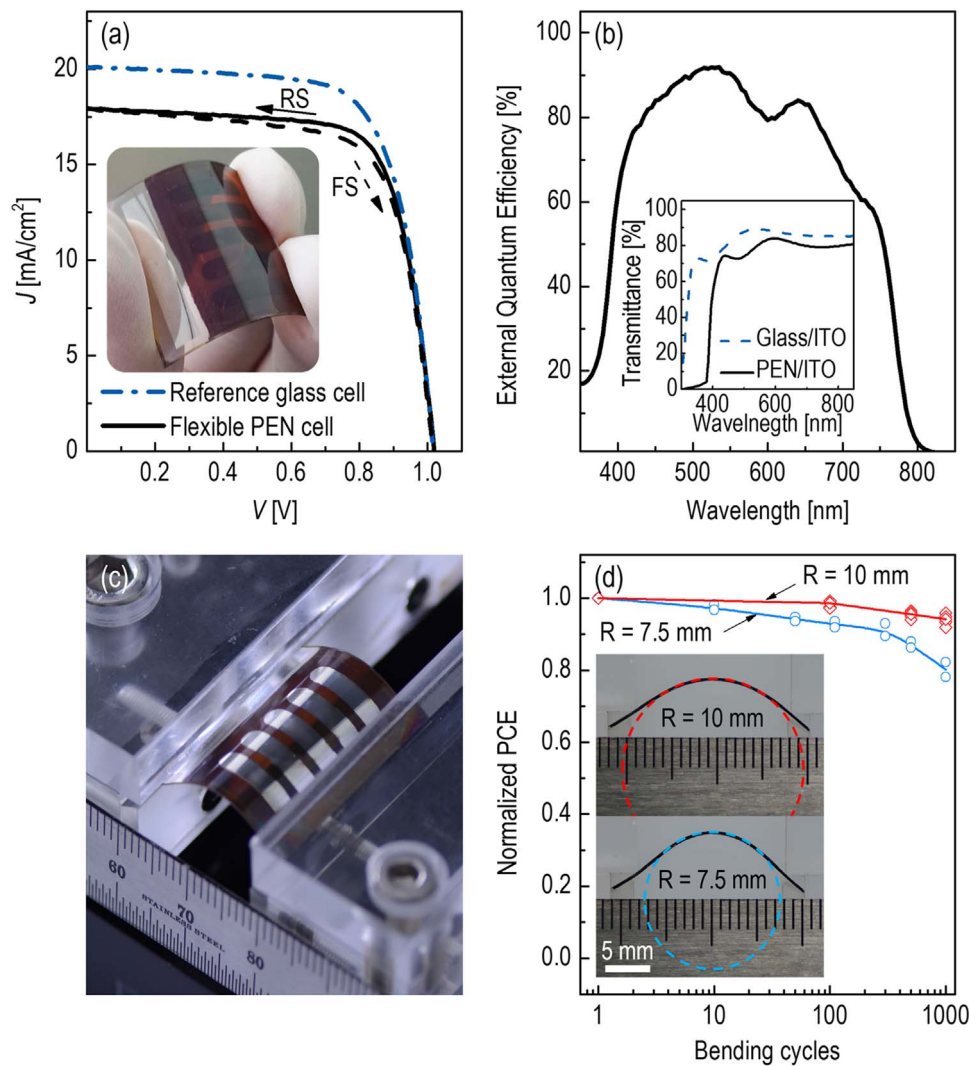


**Fig. 6.** (a)  $J$ - $V$  characteristics of the best performing psSC on ITO/PEIE/ $C_{60}$  structure with reference glass and flexible PEN substrate as inset photograph. (b) EQE characteristics of flexible psSC with inset graph of total transmittance for reference glass/ITO and flexible PEN/ITO substrates. (c) Photograph of the proposed flexible psSC placed on a custom-made cyclic bending tester under tensile strain. (d) Normalized PCE of the flexible psSCs devices as a function of bending cycles with bending radii of 7.5 and 10 mm as inset photograph. Data points in at a given cycle correspond to the values obtained from the devices (up to five in total) from a given 1"–by-1" sample. (For interpretation of the references to color in this figure, the reader is referred to the web version of this article.)

**Table 2**

Summary of the recent works on flexible perovskite solar cells.

Geometry	Substrate	Selective contact	Perovskite layer	PCE	Article	
Normal (n-i-p)	PET/ITO	TiO <sub>2</sub> ALD/TiO <sub>2</sub> UV and spiro-OMeTAD	MAPbI <sub>3-x</sub> Cl <sub>x</sub>	7.4%	[21] Giacomo et al. Adv. Energy Mater. (2015)	
	PEN/ITO	bl-TiO <sub>2</sub> /PCBM and PTAA	MAPbI <sub>3</sub>	11.1%	[22] Ryu et al. J. Mater. Chem. A. (2015)	
	PEN/ITO	TiO <sub>x</sub> and spiro-MeOTAD	MAPbI <sub>3-x</sub> Cl <sub>x</sub>	12.2%	[20] Kim et al. Energy Environ. Sci. (2015)	
	PEN/ITO	Li:SnO <sub>2</sub> and spiro-MeOTAD	MAPbI <sub>3</sub>	14.8%	[60] Park et al. Nano Energy (2016)	
	PET/ITO	am-TiO <sub>2</sub> and spiro-OMeTAD	MAPbI <sub>3-x</sub> Cl <sub>x</sub>	15.1%	[61] Yang et al. Energy Environ. Sci. (2015)	
	PEN/ITO	C <sub>60</sub> and spiro-MeOTAD	MAPbI <sub>3</sub>	15.5%	[30] Yoon et al. Energy Environ. Sci. (2016)	
	PEN/ITO	ZnO and PTAA	MAPbI <sub>3</sub>	15.6%	[62] Heo et al. J. Mater. Chem. A. (2016)	
	PET/ITO	ss-IL and spiro-OMeTAD	MAPb(I <sub>0.85</sub> Br <sub>0.15</sub> ) <sub>3</sub>	16.1%	[63] Yang et al. Adv. Mater. (2016)	
	PEN/ITO	ZSO ECL and PTAA	MAPb(I <sub>0.9</sub> Br <sub>0.1</sub> ) <sub>3</sub>	16.5%	[19] Shin et al. J. Phys. Chem. Lett. (2016)	
	PEN/ITO	PEIE/C <sub>60</sub> and spiro-OMeTAD	MAPbI <sub>3</sub>	13.3%	This work	
	Inverted (p-i-n)	PET/ITO	SOHEL2 and PCBM	MAPbI <sub>3</sub>	8.0%	[13] Lim et al. Adv. Mater. (2014)
		PET/ITO	PEDOT:PSS and PCBM	MAPbI <sub>3-x</sub> Cl <sub>x</sub>	9.2%	[16] You et al. ACS Nano (2014)
PEN/ITO		NiO <sub>x</sub> and PCBM	MAPbI <sub>3</sub>	13.4%	[64] Yin et al. ACS Nano (2016)	
PET/Ag-mesh/PH1000		PEDOT:PSS and PCBM	MAPbI <sub>3</sub>	14.2%	[65] Li et al. Nat. Commun. (2016)	
PEN/ITO		PhNa-1T and PCBM	MAPbI <sub>3</sub>	14.7%	[66] Jo et al. Adv. Funct. Mater. (2016)	

#### 4. Conclusions

In this study, efficient  $\text{CH}_3\text{NH}_3\text{PbI}_3$ -based perovskite solar cells (psSCs) were demonstrated by adopting  $\text{C}_{60}$  evaporated onto PEIE-coated ITO as an electron transporting layer (ETL) instead of mesoporous  $\text{TiO}_2$ . The PEIE layer not only served as an interfacial electron collecting layer, but also played a key role by preventing the integrity of  $\text{C}_{60}$  films from being undermined during the perovskite formation via the two-step spin-coating process. This additional benefit allowed for the growth of uniform perovskite layers free from unreacted  $\text{PbI}_2$  impurities. This led to efficient, low-hysteresis solar cells with significantly improved reproducibility. We then took advantage of the opportunity provided by the low process temperature of the proposed structure to demonstrate efficient flexible psSCs that exhibited PCE as high as 13.3%, which differed from the PCE of glass-based control cells essentially by difference in the transmittance of the substrates. Given its simplicity and compatibility with the relatively well-established two-step perovskite forming process, the proposed method is likely to speed up the realization of highly efficient flexible solar cells.

#### Acknowledgments

This work was supported by Grant No. EEW-2016-N11160015 from the Climate Change Research Hub (CRH) project of the KAIST EEW Research Center (EEW: Energy, Environment, Water and Sustainability) and by the New & Renewable Energy Core Technology Program of the Korea Institute of Energy Technology Evaluation and Planning (KETEP) granted financial resource from the Ministry of Trade, Industry and Energy (MOTIE) of the Republic of Korea (No. 20163010012200).

#### Appendix A. Supplementary material

Supplementary material associated with this article can be found in the online version at doi:10.1016/j.solmat.2016.11.031.

#### References

- [1] J.L. White, M.F. Baruch, J.E. Pander III, Y. Hu, I.C. Fortmeyer, J.E. Park, T. Zhang, K. Liao, J. Gu, Y. Yan, T.W. Shaw, E. Abelev, A.B. Bocarsly, Light-driven heterogeneous reduction of carbon dioxide: photocatalysts and photoelectrodes, *Chem. Rev.* 115 (2015), 2015, pp. 12888–12935.
- [2] W.-J. Ong, L.-L. Tan, Y.H. Ng, S.-T. Yong, S.-P. Chai, Graphitic carbon nitride ( $\text{g-C}_3\text{N}_4$ )-based photocatalysts for artificial photosynthesis and environmental remediation: are we a step closer to achieving sustainability?, *Chem. Rev.* 116 (2016) 7159–7329.
- [3] M.M. Lee, J. Teuscher, T. Miyasaka, T.N. Murakami, H.J. Snaith, Efficient hybrid solar cells based on meso-superstructured organometal halide perovskites, *Science* 338 (2012) 643.
- [4] Z. Xiao, C. Bi, Y. Shao, Q. Dong, Q. Wang, Y. Yuan, C. Wang, Y. Gao, J. Huang, Efficient, high yield perovskite photovoltaic devices grown by interdiffusion of solution-processed precursor stacking layers, *Energy Environ. Sci.* 7 (2014) 2619–2623.
- [5] J. Burschka, N. Pellet, S.-J. Moon, R. Humphry-Baker, P. Gao, M.K. Nazeeruddin, M. Grätzel, Sequential deposition as a route to high-performance perovskite-sensitized solar cells, *Nature* 499 (2013) 316.
- [6] M. Liu, M.B. Johnston, H.J. Snaith, Efficient planar heterojunction perovskite solar cells by vapour deposition, *Nature* 501 (2013) 395.
- [7] T.-B. Song, Q. Chen, H. Zhou, S. Luo, Y.M. Yang, J. You, Y. Yang, Unraveling film transformations and device performance of planar perovskite solar cells, *Nano Energy* 12 (2015) 494–500.
- [8] A. Kojima, K. Teshima, Y. Shirai, T. Miyasaka, Organometal halide perovskites as visible-light sensitizers for photovoltaic cells, *J. Am. Chem. Soc.* 131 (2009) 6050–6051.
- [9] National Center for Photovoltaics, National Renewable Energy Laboratory (NREL) efficiency chart. ([http://www.nrel.gov/ncpv/images/efficiency\\_chart.jpg](http://www.nrel.gov/ncpv/images/efficiency_chart.jpg)), 2016 (accessed 28.06.16).
- [10] J.H. Heo, S.H. Im, J.H. Noh, T.N. Mandal, C.-S. Lim, J.A. Chang, Y.H. Lee, H.-J. Kim, A. Sarkar, Md.K. Nazeeruddin, M. Grätzel, S.I. Seok, Efficient inorganic-organic hybrid heterojunction solar cells containing perovskite compound and polymeric hole conductors, *Nat. Photonics* 7 (2013) 486–491.
- [11] H. Kim, H.-S. Kim, J. Ha, N.-G. Park, S. Yoo, Empowering semi-transparent solar cells with thermal-mirror functionality, *Adv. Energy Mater.* (2016) 1502466.
- [12] X. Yin, Y. Guo, Z. Xue, P. Xu, M. He, B. Liu, Performance enhancement of perovskite-sensitized mesoscopic solar cells using Nb-doped  $\text{TiO}_2$  compact layer, *Nano Res.* 8 (2015) 1997–2003.
- [13] K.-G. Lim, H.-B. Kim, J. Jeong, H. Kim, J.Y. Kim, T.-W. Lee, Boosting the power conversion efficiency of perovskite solar cells using self-organized polymeric hole extraction layers with high work function, *Adv. Mater.* 26 (2014) 6461–6466.
- [14] K.-G. Lim, S. Ahn, Y.-H. Kim, Y. Qi, T.-W. Lee, Universal energy level tailoring of self-organized hole extraction layers in organic solar cells and organic-inorganic hybrid perovskite solar cells, *Energy Environ. Sci.* 9 (2016) 932–939.
- [15] K.-G. Lim, S. Ahn, H. Kim, M.-R. Choi, D.H. Huh, T.-W. Lee, Self-doped conducting polymer as a hole-extraction layer in organic-inorganic hybrid perovskite solar cells, *Adv. Mater. Interfaces* 3 (2016) 1500678.
- [16] J. You, Z. Hong, Y.M. Yang, Q. Chen, M. Cai, T.-B. Song, C.-C. Chen, S. Lu, Y. Liu, H. Zhou, Y. Yang, Low-temperature solution-processed perovskite solar cells with high efficiency and flexibility, *ACS Nano* 8 (2014) 1674–1680.
- [17] L. Meng, J. You, T.-F. Guo, Y. Yang, Recent advances in the inverted planar structure of perovskite solar cells, *Acc. Chem. Res.* 49 (2016) 155–165.
- [18] Z. Song, S.C. Waththage, A.B. Phillips, M.J. Heben, Pathways toward high-performance perovskite solar cells: review of recent advances in organo-metal halide perovskites for photovoltaic applications, *J. Photonics Energy* 6 (2016) 022001.
- [19] S.S. Shin, W.S. Yang, E.J. Yeom, S.J. Lee, N.J. Jeon, Y.-C. Joo, I.J. Park, J.H. Noh, S.I. Seok, Tailoring of electron-collecting oxide nanoparticulate layer for flexible perovskite solar cells, *J. Phys. Chem. Lett.* 7 (2016) 1845–1851.
- [20] B.J. Kim, D.H. Kim, Y.-Y. Lee, H.-W. Shin, G.S. Han, J.S. Hong, K. Mahmood, T.K. Ahn, Y.-C. Joo, K.S. Hong, N.-G. Park, S. Lee, H.S. Jung, Highly efficient and bending durable perovskite solar cells: toward a wearable power source, *Energy Environ. Sci.* 8 (2015) 916–921.
- [21] F.D. Giacomo, V. Zardetto, A. D'Epifanio, S. Pescetelli, F. Matteocci, S. Rizza, A.D. Carlo, S. Licoccia, W.M.M. Kessels, M. Creatore, T.M. Brown, Flexible perovskite photovoltaic modules and solar cells based on atomic layer deposited compact layers and UV-irradiated  $\text{TiO}_2$  scaffolds on plastic substrates, *Adv. Energy Mater.* 5 (2015) 1401808.
- [22] S. Ryu, J. Seo, S.S. Shin, Y.C. Kim, N.J. Jeon, J.H. Noh, S.I. Seok, Fabrication of metal-oxide-free  $\text{CH}_3\text{NH}_3\text{PbI}_3$  perovskite solar cells processed at low temperature, *J. Mater. Chem. A* 3 (2015) 3271–3275.
- [23] H.J. Snaith, A. Abate, J.M. Ball, G.E. Eperon, T. Leijtens, N.K. Noel, S.D. Stranks, J.T.-W. Wang, K. Wojciechowski, W. Zhang, Anomalous hysteresis in perovskite solar cells, *J. Phys. Chem. Lett.* 5 (2014) 1511–1515.
- [24] E.L. Unger, E.T. Hoke, C.D. Bailie, W.H. Nguyen, A.R. Bowring, T. Heumüller, M.G. Christoforo, M.D. McGehee, Hysteresis and transient behavior in current-voltage measurements of hybrid-perovskite absorber solar cells, *Energy Environ. Sci.* 7 (2014) 3690–3698.
- [25] W. Tress, N. Marinova, T. Moehl, S.M. Zakeeruddin, M.K. Nazeeruddin, M. Grätzel, Understanding the rate-dependent  $J-V$  hysteresis, slow time component, and aging in  $\text{CH}_3\text{NH}_3\text{PbI}_3$  perovskite solar cells: the role of a compensated electric field, *Energy Environ. Sci.* 8 (2015) 995–1004.
- [26] H. Moon, H. Seong, W.C. Shin, W.-T. Park, M. Kim, S. Lee, J.H. Bong, Y.-Y. Noh, B.J. Cho, S. Yoo, S.G. Im, Synthesis of ultrathin polymer insulating layers by initiated chemical vapour deposition for low-power soft electronics, *Nat. Mater.* 14 (2015) 628–635.
- [27] D. Im, H. Moon, M. Shin, J. Kim, S. Yoo, Towards gigahertz operation: ultrafast low turn-on organic diodes and rectifiers based on  $\text{C}_{60}$  and tungsten oxide, *Adv. Mater.* 23 (2011) 644–648.
- [28] B.-S. Kim, T.-M. Kim, M.-S. Choi, H.-S. Shim, J.-J. Kim, Fully vacuum-processed perovskite solar cells with high open circuit voltage using  $\text{MoO}_3/\text{NPB}$  as hole extraction layers, *Org. Electron.* 17 (2015) 102–106.
- [29] K. Wojciechowski, T. Leijtens, S. Siprova, C. Schlueter, M.T. Hörantner, J.T.-W. Wang, C.-Z. Li, A.K.-Y. Jen, T.-L. Lee, H.J. Snaith,  $\text{C}_{60}$  as an efficient n-type compact layer in perovskite solar cells, *J. Phys. Chem. Lett.* 6 (2015) 2399–2405.
- [30] H. Yoon, S.M. Kang, J.-K. Lee, M. Choi, Hysteresis-free low-temperature-processed planar perovskite solar cells with 19.1% efficiency, *Energy Environ. Sci.* 9 (2016) 2262–2266.
- [31] Y. Zhou, C. Fuentes-Hernandez, J. Shim, J. Meyer, A.J. Giordano, H. Li, P. Winget, T. Papadopoulos, H. Cheun, J. Kim, M. Fenoll, A. Dindar, W. Haske, E. Najafabadi, T.M. Khan, H. Sojoudi, S. Barlow, S. Graham, J.-L. Brédas, S.R. Marder, A. Kahn, B. Kippelen, A universal method to produce low-work function electrodes for organic electronics, *Science* 336 (2012) 327.
- [32] A.K.K. Kyaw, D.H. Wang, V. Gupta, J. Zhang, S. Chand, G.C. Bazan, A.J. Heeger, Efficient solution-processed small-molecule solar cells with inverted structure, *Adv. Mater.* 25 (2013) 2397–2402.
- [33] Y. Yi, S.J. Kang, Interfacial electronic structures between fullerene and calcium for high performance n-type organic semiconducting devices, *Thin Solid Films* 519 (2011) 3119–3122.
- [34] J.-H. Im, I.-H. Jang, N. Pellet, M. Grätzel, N.-G. Park, Growth of  $\text{CH}_3\text{NH}_3\text{PbI}_3$  cuboids with controlled size for high-efficiency perovskite solar cells, *Nat. Nanotechnol.* 9 (2014) 927–932.
- [35] J. Lee, T.-H. Han, M.-H. Park, D.Y. Jung, J. Seo, H.-K. Seo, H. Cho, E. Kim, J. Chung, S.-Y. Choi, T.-S. Kim, T.-W. Lee, S. Yoo, Synergetic electrode architecture for efficient graphene-based flexible organic light-emitting diodes, *Nat. Commun.* 7 (2016) 11791.
- [36] S. Park, H. Han, R. Kaiser, T. Werninghaus, A. Schneider, D. Drews, D.R.T. Zahn, The phototransformation of  $\text{C}_{60}$  thin films on GaAs(100) studied by *in situ* Raman spectroscopy, *J. Appl. Phys.* 84 (1998) 1340–1345.
- [37] W. Huang, J.S. Manser, P.V. Kamat, S. Ptasinska, Evolution of chemical composition, morphology, and photovoltaic efficiency of  $\text{CH}_3\text{NH}_3\text{PbI}_3$  perovskite under ambient conditions, *Chem. Mater.* 28 (2016) 303–311.

- [38] W. Ke, D. Zhao, C.R. Grice, A.J. Cimaroli, J. Ge, H. Tao, H. Lei, G. Fang, Y. Yan, Efficient planar perovskite solar cells using room-temperature vacuum-processed  $\text{CaO}$  electron selective layers, *J. Mater. Chem. A* 3 (2015) 17971–17976.
- [39] S. Venkatesan, E. Ngo, D. Khatiwada, C. Zhang, Q. Qiao, Enhanced lifetime of polymer solar cells by surface passivation of metal oxide buffer layers, *ACS Appl. Mater. Interfaces* 7 (2015) 16093–16100.
- [40] L.A.A. Pettersson, L.S. Roman, O. Inganäs, Modeling photocurrent action spectra of photovoltaic devices based on organic thin films, *J. Appl. Phys.* 86 (1999) 487–496.
- [41] J.H. Heo, D.H. Song, H.J. Han, S.Y. Kim, J.H. Kim, D. Kim, H.W. Shin, T.K. Ahn, C. Wolf, T.-W. Lee, S.H. Im, Planar  $\text{CH}_3\text{NH}_3\text{PbI}_3$  perovskite solar cells with constant 17.2% average power conversion efficiency irrespective of the scan rate, *Adv. Mater.* 27 (2015) 3424–3430.
- [42] B.R. Sutherland, S. Hoogland, M.M. Adachi, P. Kanjanaboos, C.T.O. Wong, J.J. McDowell, J. Xu, O. Voznyy, Z. Ning, A.J. Houtepen, E.H. Sargent, Perovskite thin films via atomic layer deposition, *Adv. Mater.* 27 (2015) 53–58.
- [43] D. Choi, S.-J. Hong, Y. Son, Characteristics of Indium Tin Oxide (ITO) nanoparticles recovered by lift-off method from TFT-LCD panel scraps, *Materials* 7 (2014) 7662–7669.
- [44] S.M. Jain, B. Philippe, E.M.J. Johansson, B.-W. Park, H. Rensmo, T. Edvinsson, G. Boschloo, Vapor phase conversion of  $\text{PbI}_2$  to  $\text{CH}_3\text{NH}_3\text{PbI}_3$ : spectroscopic evidence for formation of an intermediate phase, *J. Mater. Chem. A* 4 (2016) 2630–2642.
- [45] S.R. Raga, M.-C. Jung, M.V. Lee, M.R. Leyden, Y. Kato, Y. Qi, Influence of air annealing on high efficiency planar structure perovskite solar cells, *Chem. Mater.* 27 (2015) 1597–1603.
- [46] H. Xie, X. Liu, L. Lyu, D. Niu, Q. Wang, J. Huang, Y. Gao, Effect of precursor ratios and annealing on electronics structure and surface composition of  $\text{CH}_3\text{NH}_3\text{PbI}_3$  perovskite films, *J. Phys. Chem. C* 120 (2016) 215–220.
- [47] D. Bi, C. Yi, J. Luo, J.-D. Décoppet, F. Zhang, S.M. Zakeeruddin, X. Li, A. Hagfeldt, M. Grätzel, Polymer-templated nucleation and crystal growth of perovskite films for solar cells with efficiency greater than 21%, *Nat. Energy* 1 (2016) 16142.
- [48] R. Lindblad, D. Bi, B.-W. Park, J. Oscarsson, M. Gorgoi, H. Siegbahn, M. Odelius, E.M.J. Johansson, H. Rensmo, Electronic structure of  $\text{TiO}_2/\text{CH}_3\text{NH}_3\text{PbI}_3$  perovskite solar cell interfaces, *J. Phys. Chem. Lett.* 5 (2014) 648–653.
- [49] R.S. Sanchez, V. Gonzalez-Pedro, J.-W. Lee, N.-G. Park, Y.S. Kang, I. Mora-Sero, J. Bisquert, Slow dynamic processes in lead halide perovskite solar cells. Characteristic times and hysteresis, *J. Phys. Chem. Lett.* 5 (2014) 2357–2363.
- [50] H.-S. Kim, I.-H. Jang, N. Ahn, M. Choi, A. Guerrero, J. Bisquert, N.-G. Park, Control of *I-V* hysteresis in  $\text{CH}_3\text{NH}_3\text{PbI}_3$  perovskite solar cell, *J. Phys. Chem. Lett.* 6 (2015) 4633–4639.
- [51] O. Almora, I. Zarazua, E. Mas-Marza, I. Mora-Sero, J. Bisquert, G. Garcia-Belmonte, Capacitive dark currents, hysteresis, and electrode polarization in lead halide perovskite solar cells, *J. Phys. Chem. Lett.* 6 (2015) 1645–1652.
- [52] A. Dualah, T. Moehl, N. Te’trault, J. Teuscher, P. Gao, M.K. Nazeeruddin, M. Grätzel, Impedance spectroscopic analysis of lead iodide perovskite-sensitized solid-state solar cells, *ACS Nano* 8 (2014) 362–373.
- [53] H.-S. Kim, N.-G. Park, Parameters affecting *I-V* Hysteresis of  $\text{CH}_3\text{NH}_3\text{PbI}_3$  perovskite solar cells: effects of perovskite crystal size and mesoporous  $\text{TiO}_2$  layer, *J. Phys. Chem. Lett.* 5 (2014) 2927–2934.
- [54] E.J. Juarez-Perez, R.S. Sanchez, L. Badia, G. Garcia-Belmonte, Y.S. Kang, I. Mora-Sero, J. Bisquert, Photoinduced giant dielectric constant in lead halide perovskite solar cells, *J. Phys. Chem. Lett.* 5 (2014) 2390–2394.
- [55] Y. Wang, W.-Y. Rho, H.-Y. Yang, T. Mahmoudi, S. Seo, D.-H. Lee, Y.-B. Hahn, Air-stable, hole-conductor-free high photocurrent perovskite solar cells with  $\text{CH}_3\text{NH}_3\text{PbI}_3$ -NiO nanoparticles composite, *Nano Energy* 27 (2016) 535–544.
- [56] Z. Zhu, X. Zheng, Y. Bai, T. Zhang, Z. Wang, S. Xiao, S. Yang, Mesoporous  $\text{SnO}_2$  single crystals as an effective electron collector for perovskite solar cells, *Phys. Chem. Chem. Phys.* 17 (2015) 18265–18268.
- [57] S. Chavhan, O. Miguel, H.-J. Grande, V. Gonzalez-Pedro, R.S. Sánchez, E.M. Barea, I. Mora-Sero, R. Tena-Zaera, Organo-metal halide perovskite-based solar cells with  $\text{CuSCN}$  as the inorganic hole selective contact, *J. Mater. Chem. A* 2 (2014) 12754–12760.
- [58] S. Hong, J. Yoo, C. Jeon, C. kang, J. Lee, J. Ryu, B. Ahn, S. Yeo, Technologies for flexible AMOLEDs, *Inf. Disp.* 31 (2015) 6–11.
- [59] A. Laskarakis, S. Logothetidis, On the optical anisotropy of poly(ethylene terephthalate) and poly(ethylene naphthalate) polymeric films by spectroscopic ellipsometry from visible-far ultraviolet to infrared spectral regions, *J. Appl. Phys.* 99 (2006) 066101.
- [60] M. Park, J.-Y. Kim, H.J. Son, C.-H. Lee, S.S. Jang, M.J. Ko, Low-temperature solution-processed Li-doped  $\text{SnO}_2$  as an effective electron transporting layer for high-performance flexible and wearable perovskite solar cells, *Nano Energy* 26 (2016) 208–215.
- [61] D. Yang, R. Yang, J. Zhang, Z. Yang, S.F. Liu, C. Li, High efficiency flexible perovskite solar cells using superior low temperature  $\text{TiO}_2$ , *Energy Environ. Sci.* 8 (2015) 3208–3214.
- [62] J.H. Heo, M.H. Lee, H.J. Han, B.R. Patil, J.S. Yu, S.H. Im, Highly efficient low temperature solution processable planar type  $\text{CH}_3\text{NH}_3\text{PbI}_3$  perovskite flexible solar cells, *J. Mater. Chem. A* 4 (2016) 1572–1578.
- [63] D. Yang, R. Yang, X. Ren, X. Zhu, Z. Yang, C. Li, S.F. Liu, Hysteresis-suppressed high-efficiency flexible perovskite solar cells using solid-state ionic-liquids for effective electron transport, *Adv. Mater.* 28 (2016) 5206–5213.
- [64] X. Yin, P. Chen, M. Que, Y. Xing, W. Que, C. Niu, J. Shao, Highly efficient flexible perovskite solar cells using solution-derived  $\text{NiO}_x$  hole contacts, *ACS Nano* 10 (2016) 3630–3636.
- [65] Y. Li, L. Meng, Y.M. Yang, G. Xu, Z. Hong, Q. Chen, J. You, G. Li, Y. Yang, Y. Li, High-efficiency robust perovskite solar cells on ultrathin flexible substrates, *Nat. Commun.* 7 (2016) 10214.
- [66] J.W. Jo, M.-S. Seo, M. Park, J.-Y. Kim, J.S. Park, I.K. Han, H. Ahn, J.W. Jung, B.-H. Sohn, M.J. Ko, H.J. Son, Improving performance and stability of flexible planar-heterojunction perovskite solar cells using polymeric hole-transport material, *Adv. Funct. Mater.* 26 (2016) 4464–4471.